Conformational Ordering on the Growth Front of Isotactic Polypropylene Spherulite

Yuanhua Cong,[†] Zhihua Hong,[‡] Weiming Zhou,[†] Wei Chen,[†] Fengmei Su,[†] Hailong, Li,[†] Xiangyang Li,*,[†] Ke Yang,[§] Xiaohan Yu,[§] Zeming Qi,[†] and Liangbin Li*,[†,‡]

[†]National Synchrotron Radiation Laboratory and College of Nuclear Science and Technology, University of Science and Technology of China, Hefei, China

[‡]Department of Polymer Science and Engineering, CAS Key Lab of Soft Matter Chemistry, University of Science and Technology of China, Hefei, China

[§]Shanghai Synchrotron Radiation Facility, Shanghai, China

ABSTRACT: The growth front of isotactic polypropylene (iPP) spherulites is studied with series of in-situ microanalyzing techniques: conventional source infrared microspectroscopic (CS-μIR), polarized infrared microspectroscopic imaging (SR-μPIR), and scanning X-ray microdiffraction (SR-μSXRD). By SR-μSXRD, the actual growth front boundary of spherulite was clearly defined, which is the boundary observed with an optical microscope. Measurements of CS-μIR and SR-μPIR on growing spherulites reveal that a growth front layer (GFL) with high content of conformational ordered long helices exists outside the growth front of spheurlite, which has a thickness up to 30 μm above 142 °C. These long helices preferentially orient perpendicular to the radial direction of spherulite, whose growth fashion seems correlating with the growth of spherulite.

Spherulite
- Lamella crystal ··· B_{OM}
- $CORS_P$ boundary layer
- $CORS_P$
- $CORS_m$
- CORS in crystal
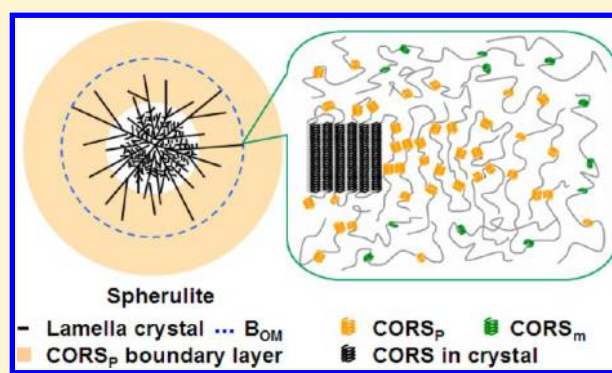
INTRODUCTION

Polymer crystallization is a fundamental challenge of polymer physics attracting broad interest from scientific and industrial community since 1960s, which however is still lack of a satisfactory molecular theory. One crucial issue but controversial about polymer crystallization is whether preordering occurs before the onset of crystallization or not.[1−10] As introduced and discussed in previous work,[11] to solve this physical question, many efforts on preordering have been conducted on either the induction period of crystallization or on the growth front of crystal. In induction period, a spinodal assisted crystallization mechanism has been deduced from scattering and spectral results,[10,12−17] which is attributed to coupling between conformational order and density fluctuation.[18] At the growth front, Strobl proposed a multistage process model, where a transient mesomorphic layer is proposed at the growth front of crystal.[1] Nevertheless, clear structural information about the preordering is still absent.

In searching for the occurrence preordering, it is more convenient to follow the growth front of crystal than to check primary nucleation, as the former provides a well-defined location to look for. Spherulite is an ideal system as a clear boundary can be tracked with optical microscopy (OM) or polarized optical microscopy (POM), which also provides rich growth front of lamellae. Conformational ordering inside growing spherulite is observed recently.[11] As inside spherulite the signal of conformational ordering is mixed with that from

crystallization, it would be more conclusive to study this phenomenon outside the growth front of spherulite where no lamellar crystal exists at all. Evidently defining the boundary line of a growing spherulite is the first step to answer the debate of preordering at the growth front of crystal, which turns out to be a nontrivial problem.

The structure of spherulite was established by the pioneer work of Bassett and co-workers with a combination of etching method and electronic microscope (EM), where the notions of dominant and subsidiary lamellae were introduced.[19−22] The continuous growth of the dominant lamellae forms a spherical skeleton, while the subsidiary lamellae fill up the space among the dominant lamellae. Because of the difference between expansion and filling processes, an extended boundary layer with dominant lamellae alone was observed in the quenched spherulite with a thickness of several micrometers.[19−29] Atomic force microscopy (AFM) was employed as an in-situ technique to track the growth front at lamellar level in real time, where the extended boundary layer with thickness comparable to that observed with EM was directly caught during growing process.[30−34] Because of the difference of refractive indices of amorphous and crystal, a clear boundary line (B_{OM} or B_{POM}) between melt and spherulite can be defined with OM or POM,

which, however, misses the detailed information on the extended boundary region.[35−40] With a high spatial resolution, synchrotron radiation X-ray microdiffraction revealed that a low-crystallinity zone with a width of 30 μm exists inside B_{POM} in the quenched isotactic polypropylene (iPP) sample, which is much wider than the extended boundary layer determined by AFM and EM.[41] Outside B_{OM}, a layer with ordered conformation was observed with Raman microscopy, which was attributed to conformational ordering rather than crystallization.[42] Though numerous descriptions on the growth front of spherulite have been proposed, a discrepancy still exists on the boundary line defined with different techniques.

In this work, microbeam wide-angle X-ray diffraction (SR-μWAXD) was first used to check the real boundary of growing spherulite. Conventional source infrared microspectroscopic (CS-μIR) and synchrotron radiation polarized infrared microspectroscopic (SR-μPIR) imaging were further employed to detect the growth fashion on the growth front. Results from the series of microscopic measurements show that outside the actual boundary of growing spherulites conformational ordered long helices are organized in a layer with a thickness of about 30 μm, which gives the direct evidence for the existence of preordering.

■ EXPERIMENTAL SECTION

High-molecular-mass iPP used in this study was kindly supplied by SABIC-Europe. It has a melt flow index about 0.3 g/10 min (230 °C/2.16 kg, ASTM D1238) and an average M_n and M_w of about 150 and 720 kg/mol, respectively. The melting point is around 165 °C.

Infrared Microspectroscopic Imaging (μIR). μIR imaging offers the possibility to combine spectral and spatial information, which is effective to explore the distribution of characteristic structure and its kinetic process.[43−45] Both CS-μIR and SR-μPIR imaging measurements were performed on IR spectroscopy and microspectroscopic imaging end-station at National synchrotron Radiation Laboratory (NSRL). The end-station equips with a Bruker HYPERION 3000 microscope coupled to Bruker IFS 66v FTIR spectrometer. With a 64 × 64 elements focal plane array (FPA) detector, 250 μm × 250 μm areas can be measured in 5 min with 128 scans and a resolution of 4 cm^{-1}. A homemade hot stage with a temperature uncertainty of ±0.1 °C is developed for the in-situ experiment. For orientation measurement with polarized beam, we took synchrotron IR source due to its high brilliance and polarized properties. Synchrotron IR radiation with an initial degree of polarization of 90% was further purified by placing a Specac KRS5 polarizer in the beam path between beam splitter and the sample, whose intensity is about 7 times higher than that of the polarized conventional source (globar source) at a spot size of 50 μm × 180 μm.

The iPP film with a thickness of ca. 200 μm was put onto a ZnSe window and heated up to 210 °C for 10 min and then cooled to 135 °C to initiate nucleation. After that sample was heated up again to the required temperature for isothermal crystallization and kept for 10 min to reach the stably growing state before growth kinetic test. IR spectra at a resolution of 4.0 cm^{-1} were immediately collected following the snapshot of optical imaging. For all experiments, the measured spectrum wavenumber range was 3900−700 cm^{-1} and 128 scans were taken for averaging. The baseline of spectra was carefully adjusted uniformly using OPUS 5.5 package. Height of peak is considered as integral intensities of the conformational bands in all of IR data in this study.

Synchrotron Radiation Scanning X-ray Microdiffraction (SR-μSXRD). SR-μSXRD based on third generation synchrotron radiation facility is suitable to explore the structure of spherulite due to its high spatial resolution and high brilliance.[46] In this work, SR-μSXRD measurement was performed at BL15U of Shanghai Synchrotron Radiation Facility (SSRF). Data from the beam profile show that the area of the microspot was 2.3 μm × 1.7 μm with a wavelength λ of

0.124 nm. The distance between the sample and the detector was 185.25 mm. The diffraction pattern was collected with Mar165 CCD. A homemade hot stage with a temperature uncertainty of ±0.1 °C was designed to combine with X-ray microdiffraction experiment. Preparation of growing spherulites was similar to IR test. OM images were first snapshot by CCD camera from the normal direction of the sample. Then it was switched to Mar165 CCD by motor for the next continuous scanning microdiffraction measurements. At each detected point, the exposure time was 4 s and scanning step was 5 μm.
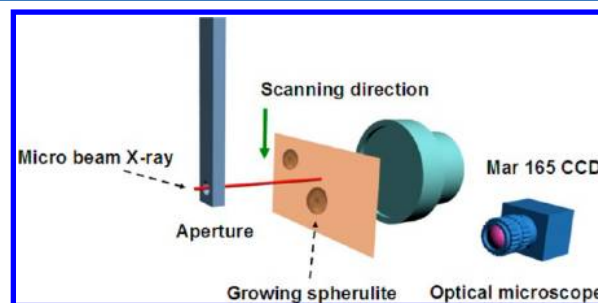

Figure 1. Schematic setup used for scanning microdiffraction measurements.

■ RESULTS

To answer the fundamental question whether preordering exists on the growth front of a spherulite, the real boundary should be determined first. A growing spherulite was studied with in situ SR-μSXRD. Considering the growth rate, the crystallization temperature was chosen to be 145 °C, which could ensure the radial growth distance of the spheurlite is less than one step size during the whole mapping process. 2-D diffraction patterns at different points along a diameter of the spherulite were obtained. Figure 2 shows the optical microscopy image of the spherulite and some selected 2-D diffraction patterns (marked with characters from A to O). Among these points, A, B, N, and O are outside the spherulite. Points A and O are 20 μm away from B_{OM}, while points B and N are 5 μm away from B_{OM}. Their corresponding diffraction patterns exhibit no visible Bragg reflections. The absence of the WAXD signal unlikely is due to the orientation. Because the typical α-form crystals own various planes of (110), (040), (130), (111), and (131), there is no orientation from which all of the diffraction patterns can disappear. Thus, the absence of the WAXD signal should be attributed to the absence of iPP crystal. Points C−M show a series of diffraction arcs which are indicative of the crystalline structures. This indicates that iPP crystal only can be detected inside the spherulite. The points C and M inside the spherulite, which are only 5 μm away from the boundary, are worth mentioning. It is well-known that a parent lamella usually induces the formation of a daughter lamella. The diffraction pattern of iPP at point C indicates that the c-axis of parent lamellae is perpendicular to the normal direction of iPP film. If daughter lamellae exist, whose (110) plane should contribute a diffraction arc in the equator direction as they have an angle of 98° with parent lamellae.[47] However, no such a diffraction arc appears, indicating the absence of daughter lamellae here. Unlike the situation in point C, the c-axis of parent lamellae in point M is parallel to the normal direction of iPP film deducing from its diffraction pattern.[47] In this case, it is difficult to deduce that there are daughter lamellae or not because the diffraction arc from (040) plane of daughter lamellae will overlap with that of the parent lamellae. But, due
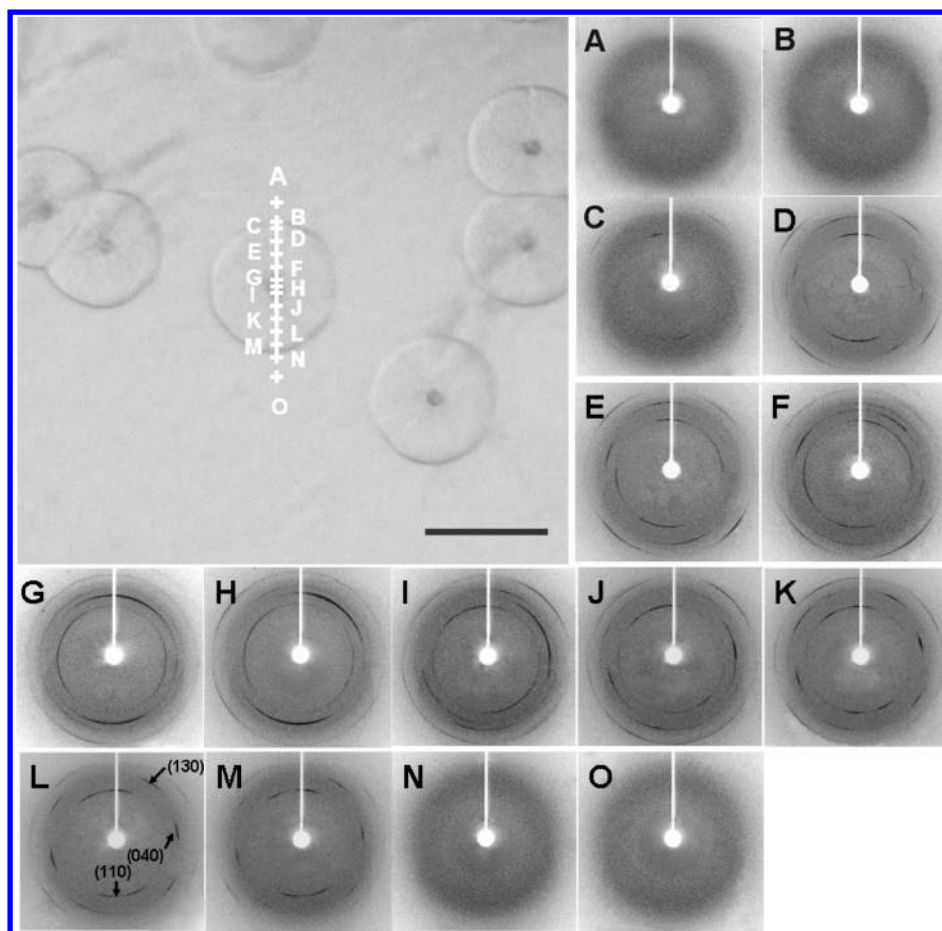
Figure 2. Optical microscope image of a single spherulite with selected incident points marked with characters from A—O and the corresponding 2-D diffraction patterns. The scale bar is 100 μm.
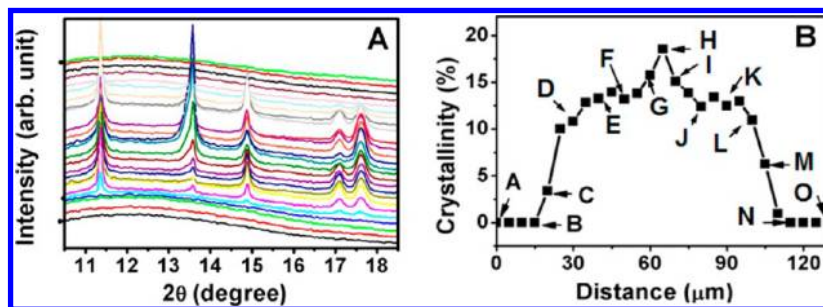

Figure 3. (A) Series of 1-D curves obtained by step scans across the spherulite. (B) Crystallinity distribution against scanning distance from A to O.

to the symmetrical characteristic of spherulite growth, it is highly possible that only parent lamellae grow in point M at the moment when the iPP spherulite was mapped by SR-μSXRD.

Figure 3A gives integrated 1-D diffraction curves at all measuring points along the diameter. Five typical diffraction peaks at 11.34°, 13.59°, 14.87°, 17.20°, and 17.52° could be indexed to the monoclinic α-crystalline form of iPP, which only emerge in inside B_{OM}. For a direct view of distribution of crystal, the crystallinity of each scanning point is calculated and plotted against distance in Figure 3B, where A–O are the same as marked in Figure 2. From point A to B, the crystallinity is zero. When the scanning point enters B_{OM}, the crystallinity increases abruptly. With the increase of mapping distance, until the center of spherulite, the crystallinity also increases. The trend of step scans from the central region to melt gives a

symmetric shape. This trend is well accorded with the one observed in the quenched spherulite by Kolb et al.,[41] in-situ scanning data from Raman microscopy by Gatos et al.,[42] and also crystallinity distribution from CS-μIR imaging by Cong et al.[11] Here, it should be pointed out that the crystallinity obtained is lower than the value commonly reported for a bulk completely crystallized iPP sample. In the study, in order to measure a single spherulite easily as seen in Figure 2, a high crystallization temperature (145 °C) was chosen to control crystal grow. During measurements, a high content of iPP melt existed, and X-ray inevitably passed though the iPP melt outside the spherulite. The high content of iPP melt (>50%) in the incident path of X-ray resulted in a significant decrease in crystallinity. With the bell-shaped curve of crystallinity in hand,
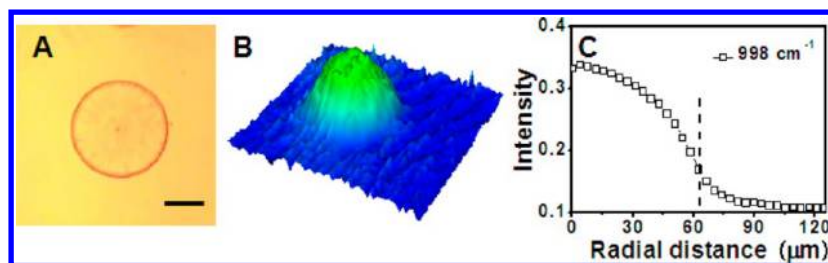
Figure 4. (A) Optical microscope image of an individual spherulite. (B) Corresponding 3-D image of intensity distributions of 998 cm^{-1} band. (C) Intensity distributions of 998 cm^{-1} band against radial distance. (The scale bar is 50 μm.)

a conclusion can be drawn that the B$_{OM}$ is the actual boundary of the growing spheurlite.

After the actual boundary has been determined, the growth fashion outside the B$_{OM}$ was directly monitored by CS-μIR imaging. A typical optical microscope image of a spherulite was snapshot in an isothermal process at 145 °C (Figure 4A). The corresponding IR spectra were also collected simultaneously. Herein, the band at 998 cm^{-1} is selected for analysis which could represent conformational ordered segments (CORS) in normal melt (CORS$_m$), preordreing (CORS$_p$), and crystal.[18,48−52] For the convenience of description, the absorption intensity of CORS at 998 cm^{-1} band of iPP melt and crystal are defined as I_{CORS-M} and I_{CORS-C}, respectively. If preordering exists, it is denoted as I_{CORS-P}. After the imaging technique treatment, the spatial distribution of intensities of 998 cm^{-1} band was obtained and presented as 3-D image in Figure 4B. The increase of height reflects the increase of intensity of the 998 cm^{-1} band. With the methodology proposed by our group,[11] we calculate the average intensities of the 998 cm^{-1} band against the radial distance of the spherulite and show it in Figure 4C. The intensity of the center of spherulite is the highest, which decreases with the increase of radial distance and reaches a plateau in the melt zone. The boundary line B$_{OM}$ determined by OM is also marked as a dashed line in Figure 4C. At the B$_{OM}$, the intensity of the 998 cm^{-1} band is obviously higher than the value of the plateau in the melt zone, which is consistent with results reported by Gatos et al.[42] Outside B$_{OM}$, the intensity of 998 cm^{-1} decreases continuously and reaches the plateau value of melt at a radial distance of around 30 μm from B$_{OM}$. With the intensity of the 998 cm^{-1} band higher than the melt, the layer with a width of 30 μm outside B$_{OM}$ contains higher concentration of the conformational ordered helices. We denoted the layer with high concentration of ordered long helices outside B$_{OM}$ as the growth front layer (GFL).

The orientation of those helices in the GFL was further checked with SR-μPIR imaging. A growing spherulite was caught during an isothermal crystallization at the temperature of 145 °C (Figure 5A). The incident SR-μPIR was only through aperture between the four-plate slits covering an area of 50 μm × 180 μm. The polarization direction of the infrared is denoted as a red double-headed arrow in Figure 5A. The corresponding contour map of 998 cm^{-1} band is shown in Figure 5B. As expected, the optical spherulitic zone or region inside B$_{OM}$ gives the highest intensity due to crystallization, while the melt zone far away from B$_{OM}$ show a lower intensity. Surprisingly, between B$_{OM}$ and the melt, the GFL has the lowest intensity, which is in contrast to that detected with CS-μIR imaging with a nonpolarized beam (Figure 4C). Evidently the low intensity of the 998 cm^{-1} band at the GFL in Figure 5B is due to orientation of helices. As the 998 cm^{-1} band has a polarization direction parallel to the helix axis[53] and the IR beam is
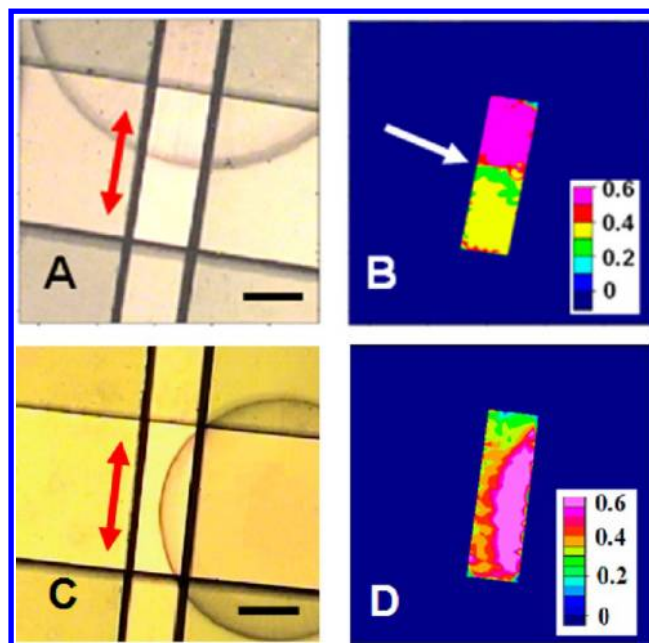

Figure 5. In-situ optical microscope image (A) and corresponding contour maps of intensity distribution of the 998 cm^{-1} band (B) of a single spherulite where the polarization direction parallel to the helix axis. In-situ optical microscope image (C) and corresponding contour maps of intensity distribution of the 998 cm^{-1} band (D) of a single spherulite where the polarization direction is perpendicular to the helix axis. (The scale bar is 50 μm.)

polarized in the radial direction of the spherulite in Figure 5A, there is only an reasonable explanation, e.g., the majority of the helices in the GFL perpendicularly to the radial axis of the spherulite. In order to further check the orientation of the helices, the polarization direction of the infrared was placed perpendicularly to the radial axis of the spherulite as shown in Figure 5C. The corresponding contour map of 998 cm^{-1} was displayed in Figure 5D. Here it should be noted that the IR information along horizontal direction can only be obtained in 50 μm range due to the limited width of SR-IR spot. It can be seen that IR intensity decreases gradually along radial direction of the spherulite. In other words, the IR intensity in the GFL layer was higher than that in melt region. From comparison of Figures 5B and 5D, it can be concluded that the helices in the GFL indeed lay perpendicularly to the radial axis of the spherulite.

The orientation of helices in the GFL is confirmed during the growth process of a spherulite at 135 °C. Optical microscope images with 5 min interval (A$_1$, A$_2$, and A$_3$ in Figure 6) exhibit the kinetic progress. The corresponding spatial distribution images of intensities of 998 cm^{-1} band (B$_1$, B$_2$, and B$_3$) are
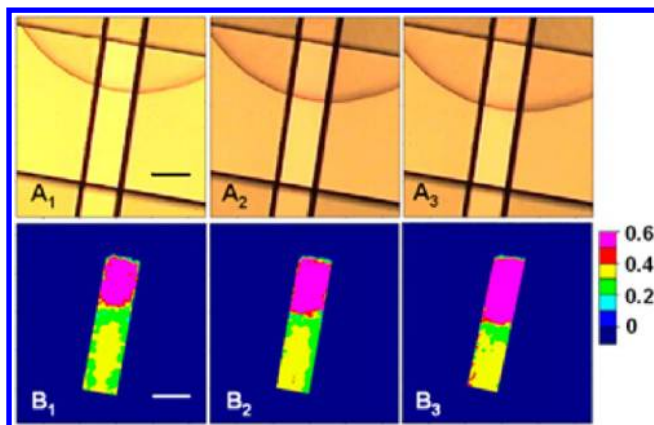
Figure 6. In-situ optical microscope images of a single spherulite (set of A) and the corresponding contour maps of intensity distribution of 998 cm^{-1} band (sets of B, 1−3 are collected at different time during isothermal crystallization at 135 °C). (The scale bar is 50 μm.)

presented in Figure 6 as 2-D contour maps. The intensity of the 998 cm^{-1} band in melt zone keeps relatively constant during the whole crystallization process, which is obviously weaker than that in the spherulitic zone. The GFL always gives the lowest intensity, though its position moves along with the growth of the spherulite. Note the region near the edges of slits also exhibits a weaker intensity, which is due to the primary intensity distribution of SR beam (Figure 6, B_1 and B_2). The intensity and orientation distribution of 998 cm^{-1} band indicate that the GFL outside B_{OM} has the following characters: (i) higher concentration of conformational ordered segments than that of melt; (ii) the helices mainly perpendicular to the radial direction of spherulite; (iii) the GFL moving outward with the growth of spherulite.

Here it should be pointed out that the appearance of spherulite may induce thickness variation and hence causes variation in IR absorbance; however, the thickness variation unlikely is responsible for the decrease of IR absorbance against radial distance shown in Figure 4C. Compared to the thickness of the sample, conformational ordering increases the absorption intensity of IR band more significantly, and the presence of crystal inside spherulite has been detected by SR-μSXRD (see Figure 2). Therefore, it is not suitable to neglect the leading role of conformational ordering in increasing the absorption intensity of IR band. More importantly, the width of the preordered zone was not determined only by CS-μIR imaging. SR-μPIR was also employed to further confirm it. Higher absorbance intensity of 998 cm^{-1} in GFL layer than that in melt zone was observed with CS-μIR imaging, while lower absorbance intensity of 998 cm^{-1} along vertical direction in

GFL layer than that in melt zone was found with SR-μPIR, which cannot be explained simultaneously by only thickness variation. Therefore, it is more reasonable to conclude that the variation of the IR band intensity against radial distance is attributed to the change in conformational ordering rather than thickness variation.

The radial growth rates of GFL and B_{OM} at different temperatures were calculated and are summarized in Figure 7A. The growth rate of B_{OM} decreases with the increase of crystallization temperature, while the radial growth rate of GFL exhibits the same trend. Within the limits of experimental error, it equals to the growth rate of B_{OM}. The average thickness of GFL layer at different crystallization temperature was further checked. Note that during the process of collecting IR spectrum (3.36 min) the target spherulite keeps growing. The thickness data at each temperature is already subtracted from the radial expansion distance of B_{OM}. As shown in Figure 7B, the thickness against temperature follows a nonmonotonic trend, which gives a bell-shaped curve with a maximum at 142 °C.

■ DISCUSSION

By combined use of OM, POM, and SR-μSXRD (see Figures 2 and 3), it was found that crystal only can be detected within the growing iPP spherulite. An abrupt change in crystallinity was observed at the spherulite surface. Different from the SR-μSXRD result, the intensity of IR peak can vary with radial distance continuously. Moreover, there exists a growth front layer near the spherulite zone where I_{CORS} is obviously larger than the plateau value of melt region (I_{CORS-M}). These extra CORS might be contributed by weak crystal or preordering. The crystal content could be lower than the detecting limit of SR-μSXRD, so that the crystal cannot be detected by SR-μSXRD but it can induce a slight increase in CORS. With iPP gel, we checked the detecting limit of SR-μSXRD. The results show crystallinity as low as 0.2% can be easily probed. If the extra absorption intensity of 998 cm^{-1} in GFL is contributed from crystal, the average crystallinity in GFL is estimated to be 1.8%. Thus, if crystal exist indeed in the GFL, it can be captured by SR-μSXRD. Therefore, these extra CORS only can be attributed to the so-called preordering.

The orientation of CORS in GFL is detected with polarized SR-μPIR imaging, which reveals that these CORS pack with a preferring orientation perpendicular to radial axis of the spherulite (Figures 5B and 6). This indicates that not only conformational ordering but also orientational ordering occurs at the growth front of spherulite. Combining the results from CS-μIR and SR-μPIR, a molecular picture of the preordering in the GFL is constructed in Figure 8, which contains both intramolecular conformational order and intermolecular
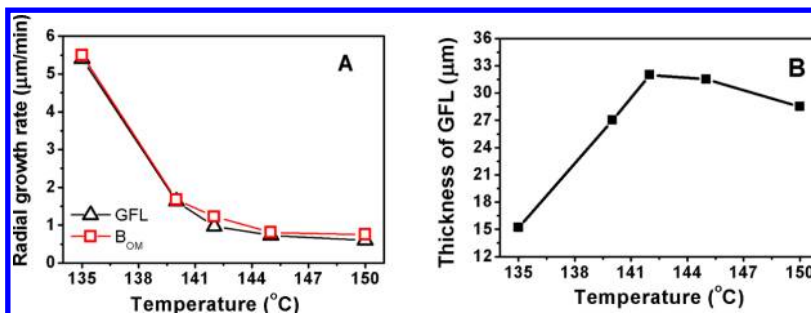

Figure 7. (A) Radial growth rate of GFL and B_{OM} against temperature. (B) Thickness of GFL layer against crystallization temperature.
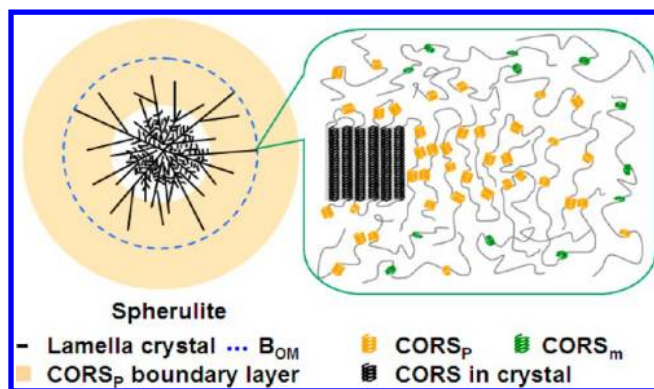
Figure 8. A scheme of a growing spherulite with a preordering growth front layer.

orientational order. This picture is rather close to the growing mesomorphic layer proposed by Strobl.[1] Nevertheless, without the thermodynamic information on the GFL, it seems difficult to answer the question that whether the preordering is a thermodynamic phase or just a kinetic pathway like a diffusion growth surface.

The orientation of CORS (Figure 6), the radial growth rate, and the thickness of GFL (Figure 7) suggest that the preordering in GFL is correlated with the growth of spherulite or lamellar crystal. The growth surface of lamellar crystal may serve as a substrate to induce conformational ordering in GFL, which can explain the same preparing orientation of CORS in both crystal and in GFL. Note even with a simple solid surface, polymer segments also prefer to lay parallel on the surface. However, the thickness of GFL is up to 30 μm. It seems unlikely a diffuse growth surface can reach such a long distance. Without introducing a thermodynamic phase, it is also difficult to imagine that a solid surface can induce a preferring segmental orientation up to 30 μm, which is normally in the scale of nanometer or radial of gyration. The temperature dependence of GFL thickness is a more decisive evidence to support that the preordering is a phase rather a kinetic pathway. As shown in Figure 7B, the thickness of GFL shows a nonmonotonic trend with crystallization temperature with a maximum at 142 °C. If the preordering is just a kinetic pathway, one would expect the thickness of GFL is a monotonic function of temperature, as a "kinetic preordering" without local minimum in energy landscape cannot stop, which should follow the same thermodynamic behavior of crystallization. The nonmonotonic trend of GFL thickness means the preordering has a relatively independent thermodynamic behavior. As the steady growth rate from molten region (G_{M-P}) and the growth rate of crystal from preordering (G_{P-C}) are the same, which keeps the thickness of GFL as constant during growth, the existence of the GFL can be attributed to three different pathways. (i) Preordering takes before crystallization. In this approach, though $G_{M-P} = G_{P-C}$, as the growth time is different, it is possible to generate the GFL with certain thickness. (ii) Before reaching steady growth, the initial growth rates of two processes are different with $G_{M-P} > G_{P-C}$. (iii) A constraint is imposed by lamellar crystal, which restricts preordering growing in a limit distance from its surface. (i) and (ii) support that the preordering in GFL is a thermodynamic metastable phase. (iii) is possible to be assigned as diffusive growth surface, but a kinetic pathway cannot explain the existence of a maximum thickness of GFL versus temperature

as discussed before. If the preordering in GFL takes an epitaxial growth approach from lamellar crystal (which is highly possible as supported by the orientation of CORS), a constraint from lamellar crystal on the thickness of GFL seems logic. Thus, though it is not clear which pathway takes the leading role in the formation GFL, the three pathways seems reaching the same conclusion that the preordering with conformational and orientational orders in GFL is more likely a thermodynamic metastable phase as Strobl proposed.

CONCLUSIONS

In summary, a series of microscopic and imaging techniques were explored to check the growth fashion on the growth front of iPP spherulite. Results from SR-μSXRD unambiguously revealed that B_{OM} is the real boundary of growing spherulite. Different from previous work in ref 11, herein emphasis is directly on the growth front. Surprisingly, CR-μPIR exhibits that a layer with a thickness up to 30 μm exists outside the growth front of spherulite, which owns a higher concentration of CORS. Polarized SR-μPIR further shows that these CORS segments are oriented and perpendicular to the radial direction. All of the data clearly demonstrate that preordering exists on the growth front of iPP spherulite.

AUTHOR INFORMATION

Corresponding Author
*E-mail: author:lixy81@ustc.edu.cn (X.L.); lbli@ustc.edu.cn (L.L.).

REFERENCES

(1) Strobl, G. *Eur. Phys. J. E* **2000**, *3* (2), 165−183.
(2) Lotz, B. *Eur. Phys. J. E* **2000**, *3* (2), 185−194.
(3) Muthukumar, M. *Eur. Phys. J. E* **2000**, *3* (2), 199−202.
(4) Li, L. B.; de Jeu, W. H. Flow-induced mesophases in crystallizable polymers. In *Interphases and Mesophases in Polymer Crystallization II*; Abe, A., Ed.; Springer: Berlin, 2005; Vol. *181*, pp 75−120.
(5) Point, J. J.; Rault, J.; Hoffman, J. D.; Kovacs, A. J.; Mandelkern, L.; Wunderlich, B.; Dimarzio, E. A.; Degennes, P. G.; Klein, J.; Ball, R. C.; Flory, P. J.; Yoon, D. Y.; Guttman, C. M.; Khoury, F.; Voigtmartin, I.; Bassett, D. C.; Frank, W. F. X.; Atkins, E. D. T.; Booth, C.; Uhlmann, D. R.; Grubb, D. T.; Magill, J. H.; Vesely, D.; Keller, A.; Krimm, S.; Samulski, E. T.; Calvert, P. D.; Fischer, E. W.; Stamm, M.; Geil, P. H.; Ullman, R.; Rys, F.; Rigby, D.; Stepto, R. F. T.; Windle, A. H.; Dill, K. A.; Hearle, J. W. S.; Hendra, P. J.; Ward, I. M.; Stejny, J.; Barham, P. J.; Pennings, A. J.; Posthumadeboer, A. *Faraday Discuss.* **1979**, *68*, 365−490.

(6) Hoffman, J. D.; Miller, R. L. *Polymer* **1997**, *38* (13), 3151−3212.

(7) Sadler, D. M.; Gilmer, G. H. *Phys. Rev. Lett.* **1986**, *56* (25), 2708−2711.

(8) Cheng, S. Z. D.; Li, C. Y.; Zhu, L. *Eur. Phys. J. E* **2000**, *3* (2), 195−197.

(9) Strobl, G. *Prog. Polym. Sci.* **2006**, *31* (4), 398−442.

(10) Kaji, K.; Nishida, K.; Kanaya, T.; Matsuba, G.; Konishi, T.; Imai, M. Spinodal crystallization of polymers: Crystallization from the unstable melt. In *Interphases and Mesophases in Polymer Crystallization III*; Allegra, G., Ed.; Springer: Berlin, 2005; Vol. *191*, pp 187−240.

(11) Cong, Y. H.; Hong, Z. H.; Qi, Z. M.; Zhou, W. M.; Li, H. L.; Liu, H.; Chen, W.; Wang, X.; Li, L. B. *Macromolecules* **2010**, *43* (23), 9859−9864.

(12) Matsuba, G.; Kaji, K.; Nishida, K.; Kanaya, T.; Imai, M. *Macromolecules* **1999**, *32* (26), 8932−8937.

(13) Heeley, E. L.; Poh, C. K.; Li, W.; Maidens, A.; Bras, W.; Dolbnya, I. P.; Gleeson, A. J.; Terrill, N. J.; Fairclough, J. P. A.; Olmsted, P. D.; Ristic, R. I.; Hounslow, M. J.; Ryan, A. J. *Faraday Discuss.* **2003**, *122*, 343−361.

(14) Heeley, E. L.; Maidens, A. V.; Olmsted, P. D.; Bras, W.; Dolbnya, I. P.; Fairclough, J. P. A.; Terrill, N. J.; Ryan, A. J. *Macromolecules* **2003**, *36* (10), 3656−3665.

(15) Ryan, A. J.; Fairclough, J. P. A.; Terrill, N. J.; Olmstead, P. D.; Poon, W. C. K. *Faraday Discuss.* **1999**, *112*, 13−29.

(16) Imai, M.; Kaji, K.; Kanaya, T. *Macromolecules* **1994**, *27* (24), 7103−7108.

(17) Matsuba, G.; Kanaya, T.; Saito, M.; Kaji, K.; Nishida, K. *Phys. Rev. E* **2000**, *62* (2), R1497−R1500.

(18) Olmsted, P. D.; Poon, W. C. K.; McLeish, T. C. B.; Terrill, N. J.; Ryan, A. J. *Phys. Rev. Lett.* **1998**, *81* (2), 373−376.

(19) Bassett, D. C.; Keller, A.; Mitsuhashi, S. *J. Polym. Sci., Part A: Gen. Pap.* **1963**, *1* (2), 763.

(20) Bassett, D. C. *Principles of Polymer Morphology*; Cambridge University Press: New York, 1981.

(21) Bassett, D. C.; Olley, R. H. *Polymer* **1984**, *25* (7), 935−943.

(22) Bassett, D. C.; Vaughan, A. S. *Polymer* **1985**, *26* (5), 717−725.

(23) Keller, A.; Sawada, S. *Makromol. Chem.* **1964**, *74*, 190−221.

(24) Bassett, D. C.; Hodge, A. M.; Olley, R. H. *Proc. R. Soc. London, Ser. A* **1981**, *377* (1768), 39.

(25) Olley, R. H.; Bassett, D. C. *Polymer* **1989**, *30* (3), 399−409.

(26) Bassett, D. C. *Philos. Trans. R. Soc., A* **1994**, *348* (1686), 29−43.

(27) Li, J. X.; Ness, J. N.; Cheung, W. L. *J. Appl. Polym. Sci.* **1996**, *59* (11), 1733−1740.

(28) Li, J. X.; Cheung, W. L. *J. Appl. Polym. Sci.* **1999**, *72* (12), 1529−1538.

(29) Bassett, D. C. *J. Macromol. Sci., Part B: Phys.* **2003**, *B42* (2), 227−256.

(30) Li, L.; Chan, C. M.; Li, J. X.; Ng, K. M.; Yeung, K. L.; Weng, L. T. *Macromolecules* **1999**, *32* (24), 8240−8242.

(31) Hobbs, J. K.; McMaster, T. J.; Miles, M. J.; Barham, P. J. *Polymer* **1998**, *39* (12), 2437−2446.

(32) Li, L.; Ng, K. M.; Chan, C. M.; Feng, J. Y.; Zeng, X. M.; Weng, L. T. *Macromolecules* **2000**, *33* (15), 5588−5592.

(33) Li, L.; Chan, C. M.; Yeung, K. L.; Li, J. X.; Ng, K. M.; Lei, Y. G. *Macromolecules* **2001**, *34* (2), 316−325.

(34) Jiang, Y.; Yan, D. D.; Gao, X.; Han, C. C.; Jin, X. G.; Li, L.; Wang, Y.; Chan, C. M. *Macromolecules* **2003**, *36* (10), 3652−3655.

(35) Hafele, A.; Heck, B.; Kawai, T.; Kohn, P.; Strobl, G. *Eur. Phys. J. E* **2005**, *16* (2), 207−216.

(36) Hafele, A.; Heck, B.; Hippler, T.; Kawai, T.; Kohn, P.; Strobl, G. *Eur. Phys. J. E* **2005**, *16* (2), 217−224.

(37) Keller, A. *J. Polym. Sci.* **1955**, *17* (84), 291−308.

(38) Keith, H. D.; Padden, F. J. *J. Polym. Sci.* **1959**, *39* (135), 101−122.

(39) Hutter, J. L.; Bechhoefer, J. *Phys. Rev. E* **1999**, *59* (4), 4342−4352.

(40) Varga, J. *J. Mater. Sci.* **1992**, *27* (10), 2557−2579.

(41) Kolb, R.; Wutz, C.; Stribeck, N.; von Krosigk, G.; Riekel, C. *Polymer* **2001**, *42* (12), 5257−5266.

(42) Gatos, K. G.; Minogianni, C.; Galiotis, C. *Macromolecules* **2007**, *40* (4), 786−789.

(43) Bhargava, R.; Wall, B. G.; Koenig, J. L. *Appl. Spectrosc.* **2000**, *54* (4), 470−479.

(44) Lasch, P.; Naumann, D. *Biochim. Biophys. Acta, Biomembr.* **2006**, *1758* (7), 814−829.

(45) Benning, L. G.; Phoenix, V. R.; Yee, N.; Konhauser, K. O. *Geochim. Cosmochim. Acta* **2004**, *68* (4), 743−757.

(46) Riekel, C.; Davies, R. J. *Curr. Opin. Colloid Interface Sci.* **2005**, *9* (6), 396−403.

(47) Nozue, Y.; Shinohara, Y.; Ogawa, Y.; Sakurai, T.; Hori, H.; Kasahara, T.; Yamaguchi, N.; Yagi, N.; Amemiya, Y. *Macromolecules* **2007**, *40* (6), 2036−2045.

(48) Zhu, X. Y.; Yan, D. Y.; Fang, Y. P. *J. Phys. Chem. B* **2001**, *105* (50), 12461−12463.

(49) Zerbi, G.; Zamboni, V.; Ciampelli, F. *J. Polym. Sci., Part C: Polym. Symp.* **1964**, *7*, 141.

(50) Geng, Y.; Wang, G.; Cong, Y.; Bai, L.; Li, L.; Yang, C. *Macromolecules* **2009**, *42* (13), 4751−4757.

(51) An, H. N.; Li, X. Y.; Geng, Y.; Wang, Y. L.; Wang, X.; Li, L. B.; Li, Z. M.; Yang, C. L. *J. Phys. Chem. B* **2008**, *112* (39), 12256−12262.

(52) An, H. N.; Zhao, B. J.; Ma, Z.; Shao, C. G.; Wang, X.; Fang, Y. P.; Li, L. B.; Li, Z. M. *Macromolecules* **2007**, *40* (14), 4740−4743.

(53) McDonald, M. P.; Ward, I. M. *Polymer* **1961**, *2* (3), 341−355.